ELSEVIER

Nuclear Instruments and Methods in Physics Research A 463 (2001) 227–249

NUCLEAR INSTRUMENTS & METHODS IN PHYSICS RESEARCH Section A

www.elsevier.nl/locate/nima

Simulation and analysis of pulse shapes from highly segmented HPGe detectors for the γ-ray tracking array MARS

Th. Kröll*, D. Bazzacco

Dipartimento di Fisica and INFN, Sezione di Padova, Via Marzolo 8, 35131 Padova, Italy

Received 1 June 2000; received in revised form 2 October 2000; accepted 24 October 2000

Abstract

A flexible program to calculate the pulse shapes from highly segmented HPGe detectors of various geometrical shapes has been developed. Signals originating from single points of interaction in both the quasi-true-coaxial and the closed-end part of the detector are discussed. In order to present the main features of these signals, we have introduced simplified characteristic curves. These curves are analysed with regard to the application of pulse shape analysis for three-dimensional position determination in detectors for a γ-ray tracking array. © 2001 Elsevier Science B.V. All rights reserved.

PACS: 29.40.−n; 29.40.Gx; 29.40.Wk

Keywords: Segmented HPGe detectors; Pulse shape analysis; γ-ray tracking

1. Introduction

Much of our knowledge about the structure of the nucleus is based on the spectroscopy of γ-rays. Large-volume high-purity Germanium crystals (HPGe) with semi-coaxial geometry, offering very good energy resolution and reasonable efficiency, are the most advanced detectors to measure γ-rays. To achieve a good total detection efficiency, large numbers of these detectors are arranged to 4π-arrays like GASP [1], EUROBALL [2], or GAMMASPHERE [3]. The high granularity of these arrays also avoids multiple hits in high multiplicity experiments and enables a Doppler correction of the energies of the γ-rays. In order to improve the peak-to-total ratio, each detector, single or composite, is surrounded by an Anti-Compton (AC) shield, made of a heavy scintillator like BGO. An event in the Ge is rejected by a veto, if the AC shield detects a γ-ray scattered out of the Ge. As a consequence of these shields, only approximately one-half of 4π can be covered by Ge. Therefore, the total efficiency of such an AC suppressed array is limited considerably to values around 10%.

To overcome this limitation, the concept of a γ-ray tracking array was proposed [4]. The complete solid angle will be covered by Ge detectors, and γ-rays scattered from one detector to another will not be suppressed anymore but recovered by reconstructing their scattering path (tracking). A

*Corresponding author. Present address: INFN, LNL, Via Romea 4, 35020 Legnaro, Italy. Tel.: +39-49-8068377; fax: +39-49-641925.

E-mail address: thorsten.kroell@lnl.infn.it (T. Kröll).

0168-9002/01/$ - see front matter © 2001 Elsevier Science B.V. All rights reserved.
PII: S0168-9002(01)00208-X

tracking array must consist of detectors enabling position determination of interactions with good spatial resolution. The position sensitivity can be achieved with detectors electrically segmented into two dimensions on the outer or inner contact, which is a progress in segmentation technology made available recently.

The major goal of such an array is the combination of both high photopeak efficiency (> 40%) and peak-to-total ratio (> 60%). The high performance is intended to be maintained also for events with high multiplicity of γ-rays. It is this unique capability which will allow the search for extremely weak reaction channels and experiments with weak beam intensities (e.g. radioactive beams) addressing open questions and new kinds of physics in nuclear structure, astrophysics, and fundamental interactions. The γ-ray tracking technique used to localise and analyse unknown sources of γ-rays has also possible applications in other fields like γ-ray astronomy or medical γ-ray imaging. Currently, there are two such projects under examination: GRETA (LBNL, Berkeley) [4,5] and MARS (Sezione di Padova and Sezione di Milano of the INFN, Laboratori Nazionali di Legnaro (LNL), and Politecnico di Milano) [6,7]. The project MARS—Mini ARray of Segmented detectors—is the Italian effort, as a part of a European TMR network [8], to explore the feasibility of building a γ-ray tracking array.

The complete process of γ-ray tracking consists of two steps with the first providing the input to the second: (a) identification of all interaction points providing deposited energy and three-dimensional position, and (b) reconstruction of the scattering path for each γ-ray, i.e. the actual tracking. To achieve a reasonable efficiency of the tracking algorithms, it appears that the interaction points are to be needed within a positional resolution of some mm; the efficiency of the tracking algorithms depends on this value sensitively [9–11].

The positions of the interaction points of the γ-rays can be determined analysing the pulse shape of the signals induced on the electrodes of the detector during the charge collection. The free charge carriers generated at the interaction points drift towards the electrodes under the influence of the electric field. The potential that the charges traverse along their path is reflected in the shape of the signals. Once the potential is known the measured shape can be used in order to deduce the initial interaction point. First applications based on the analysis of pulse shapes have enabled a better energy resolution, an improved Doppler correction of the γ-rays, a suppression of background events originating from β-decays and cosmic rays, or an enhanced peak-to-total ratio by Compton suppression (e.g. see recent Refs. [12–15], further references therein).

The main breakthrough towards the feasibility of a tracking array came when it was realised that, beside a net signal in the segment which collects the charge generated by an interaction, also transient signals in the neighbouring segments are induced [4,16]. The analysis of both the net charge signals and the transient signals allows to determine the positions of the interactions with a higher resolution than the segment size (which, with the current status of detector technology cannot be smaller than a few square cm). Since the segmentation is only in two dimensions, the third coordinate, which is for a semi-coaxial detector the radial coordinate, has to be determined in any case from the pulse shape [13].

The response of such a detector operated in a position sensitive mode, i.e. the set of signals from its segments, depends obviously on the detector geometry. The understanding of this response is the necessary fundament to investigate the feasibility of pulse shape analysis for tracking. The shape of the crystal as well as number, size, and arrangement of the segments have to be chosen so that the analysis of the shapes of the signals yields the positional information within the desired resolution. As a necessary step on the way to a γ-ray tracking array, therefore extensive simulation calculations have to be performed in order to study these dependences. In this frame, we have developed a program package to simulate the pulse shapes for various detector geometries. In Section 2, we will describe the technical details of our simulation calculations.

The basic properties of pulse shapes from highly segmented HPGe detectors are presented in Section 3, considering the specific $(6 \times 4 + 1)$-layout

for the different segments of the MARS prototype detector. In this paper, we focus on the discussion of the response of this detector to single interactions.

2. Details of the pulse shape calculations

At every point of interaction of the incident γ-ray with the detector crystal, energy, in the first instance, is transferred to an electron. Since this energy is less than several hundred keV per interaction for γ-rays with energies less than 1 MeV, the primary electron is stopped within a range <1 mm. Its energy is absorbed step by step by producing free charge carrier pairs of electrons and holes. From this, we usually assume that an interaction generates all charge carriers within a pointlike volume.

The signals at the contacts of a Ge detector are induced by the movement of the free charge carriers, which in its turn, is caused by the electric field inside the active volume of the detector. The active volume is the depleted region of the reverse biased Ge diode.

In our approach in calculating pulse shapes, we developed two programs. The first program computes the potential inside the detector and from this derives the electric field. The second program calculates the pulse shape using the results of the first.

The potential in a HPGe detector is given by the solution of Poisson's differential equation:

$$\Delta\Phi = -\frac{\rho}{\varepsilon} \tag{1}$$

where $\varepsilon = \varepsilon_r\varepsilon_0$ is the dielectric constant of Ge. The intrinsic space charge density $\rho = \pm e\ N_{A/D}$ (the sign depends on whether it is a p- or n-type detector, e is the elementary charge, and $N_{A/D}$ is the density of acceptors or donors, respectively), is the only free parameter which enters the calculations. We assume this space charge to be distributed homogeneously throughout the complete active volume of the detector, although in real detectors there is usually a gradient in space charge density along the crystal. It is clear that the real distribution could be easily taken into account if it would be known for our particular detector (in the program an individual value for the space charge density can be assigned to every node of the grid).

Since an analytical solution exists only for a true-coaxial geometry [17,18], Eq. (1) has to be solved numerically. A common approach to solve partial differential equations on arbitrary geometries is the finite element method (FEM) and in this work we used the computer program package Diffpack [19]. Using cubic tri-linear elements, the solution of Eq. (1) between the nodes of one finite element is approximated with a linear function.

For our calculations we assumed values typical for large volume HPGe detectors used in inbeam γ-ray spectroscopy: n-type Ge ($N_D = 10^{10}$ cm^{-3}); a crystal with a radius of 3.75 cm and a length of 10 cm; an inner hole of 8.5 cm length and a radius of 0.5 cm. A reverse bias of 4500 V is applied to the detector, the sign depending on whether the bias is applied to the inner, as it will be done in practice (positive bias), or to the outer contact (negative bias). The solution of Eq. (1) is, of course, the same for both possibilities. The realistic FEM-model of this detector consists of $\approx$ 150 000 finite elements (Fig. 1). The spatial precision of the grid is typically 1–2 mm for the radial coordinate r and longitudinal coordinate z. For the azimuthal

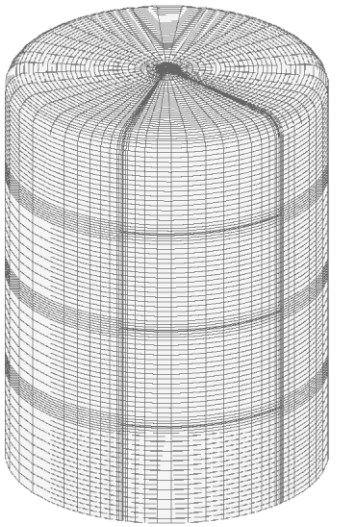

Fig. 1. FEM-model of a cylindrical detector with $(6 \times 4 + 1)$-layout of the segments.

angle φ the precision is <1–10°, depending on the region in the detector (see below). Around the borders of the segments the grid has its highest precision. The gap between the segments is chosen to be 0.5 mm. The edge of the front face and the end of the inner hole are bulletised, as in the case of a real detector.

Taking into account the obtained electric field, the pulse shapes can be calculated from the movement of charge carriers. Their drift velocity strongly depends on the electric field with a different dependence for electrons and holes. The direction of the drift velocity is simply given by the direction of the electric field, while its value is derived from a well established parametrisation [17,20,21]. It is known that the actual value of the drift velocity slightly depends also on the crystallographic orientation of the Ge single crystal [21,22]. Although this can be easily taken into account in the program, we have decided to neglect it in the present discussion as it introduces an extra level of complication which would obscure the general results.

The notation used in the following is such that the index i refers to the segment and the index c distinguishes between electrons and holes which move from the point of interaction $\boldsymbol{r}_0$ to different directions where different electric fields act on them. The drifting carriers partially charge or discharge the crystal capacitances $C_{\mathrm{det},i}$ of the segment i versus the inner contact. The differential charge $\mathrm{d}Q_{\mathrm{c},i}$ $(= I_{\mathrm{c},i}\ \mathrm{d}t)$ (the capacitances serve as current sources) which is induced at the contacts by the movement of the charge carriers q_{c} from $\boldsymbol{r}_{\mathrm{c}}$ to $\boldsymbol{r}_{\mathrm{c}} + \mathrm{d}\boldsymbol{r}_{\mathrm{c}}$ is given by

$$\mathrm{d}Q_{\mathrm{c},i} = \frac{q_{\mathrm{c}}\boldsymbol{E}_{\mathrm{W},i}(\boldsymbol{r}_{\mathrm{c}})\,\mathrm{d}\boldsymbol{r}_{\mathrm{c}}}{V_0} \tag{2}$$

where V_0 is the reverse bias applied to the detector. Since we focus on single interactions, the charges q_{c} are normalised to ± 1.

The *weighting fields* $\boldsymbol{E}_{\mathrm{W},i}(\boldsymbol{r})$ are a technique to treat mathematically the capacitive coupling between the segments based on Green's reciprocity theorem; a formulation related to its application on radiation detectors can be found e.g. in Refs. [16,23]. These artificial fields are calculated as the gradients of the *weighting potentials* $\Phi_{\mathrm{W},i}(\boldsymbol{r})$, which are solutions of Laplace's equation (Eq. (1) with $\rho = 0$) applying the reverse bias only to the one segment i under consideration, which will be referenced in the following as the *sensing segment*, and grounding all other segments.

The step $\mathrm{d}\boldsymbol{r}_{\mathrm{c}}$ is obtained by first-order integration of the drift velocity:

$$\mathrm{d}\boldsymbol{r}_{\mathrm{c}} = \boldsymbol{v}_{\mathrm{c}}(E(\boldsymbol{r}_{\mathrm{c}}))\,\mathrm{d}t. \tag{3}$$

Technically, the integration in Eq. (2) is simplified by using

$$\boldsymbol{E}_{\mathrm{W},i}(\boldsymbol{r}_{\mathrm{c}})\ \mathrm{d}\boldsymbol{r}_{\mathrm{c}} \approx \Phi_{\mathrm{W},i}(\boldsymbol{r}_{\mathrm{c}} + \mathrm{d}\boldsymbol{r}_{\mathrm{c}}) - \Phi_{\mathrm{W},i}(\boldsymbol{r}_{\mathrm{c}}) \tag{4}$$

avoiding the explicit calculation and memory consuming storage of each $\boldsymbol{E}_{\mathrm{W},i}(\boldsymbol{r}_{\mathrm{c}})$. Since we use linear finite elements, this approximation is numerically exact.

The complete output signal of the charge sensitive preamplifier is given by the sum of the signals caused by the movement of both the electrons and the holes:

$$V(t + \mathrm{d}t) \propto Q(t + \mathrm{d}t) = Q(t) + \mathrm{d}Q_{\mathrm{e}} + \mathrm{d}Q_{\mathrm{h}}. \tag{5}$$

This procedure, in fact, is a first-order integration over the current $I_{\mathrm{c=e/h}}$ in the detector. Eq. (2) have to be integrated until each charge carrier reaches its contact. For the numerical integration we use a time step of 1 ns suitable for the size of the grid. The response function of the preamplifier and the electronic noise are not considered at the present status of the discussion, but they will have to be included for a comparison with measured pulses. As already mentioned earlier and as it will become clearer in the following, there are two main kinds of signals. The signal from the sensing segment is a *net charge signal* if the charge carriers drift eventually towards the contact of this segment. Otherwise, it is a *transient signal* whose integrated charge is zero. The sum of the signals from all segments is, of course, identical to the signal from a detector without segmentation, as the sum of currents flowing into or out of the segments equals the current within the detector (Kirchhoff's law), and the latter is independent of the segmentation.

For practical reasons, throughout this paper we will use the following nomenclature for the segments: vertical columns parallel to the z-axis of the detector are named *sectors*, while horizontal

layers are called *slices*. Therefore, one particular segment is one sector of one slice. Taking into account the cylindrical symmetry of the detector, the sectors of each slice are equivalent. Hence, only *one* sector per slice has to be calculated. The grid within this sector and the surrounding area of half the angular size of the two adjacent sectors (i.e. the most interesting zone because the weighting fields do not extend further) has a more detailed grid than the rest of the detector. The other sectors can be treated by rotating the weighting fields or, what is practically easier, the actual position of the charge carriers. Since the weighting potentials in the closed-end cap are extended more widely, the complete cap is calculated with the more detailed grid, as it can be seen in Fig. 1. The drift velocity is always calculated by rotating the actual position to the sector with the more detailed grid. These procedures reduce both the necessary number of finite elements in the grid and the actual number of segments to be calculated, and hence the complete computing time to calculate the FEM-grid and for all needed sensing segments the weighting potentials.

The average computing time of the program to calculate the pulse shapes is roughly 0.5–1 s (on a 10 SPEC95 machine) per interaction and per segment, depending mainly on the number of nodes in the grid and, of course, the length of the drift path. Since for the development of algorithms for pulse shape analysis some 10 000 pulses are needed, the increase in computing efficiency was also a major part of development of this program.

In this paper we discuss only segments on the outer surface of the detector, but the program allows to place slices as well on the inner contact. Starting from the basic closed-end cylindrical shape, the crystal can be tapered or "deformed" to any other shape, like a hexagonal shape or the different hexaconical shapes which are used for CLUSTER capsules [24] or the GRETA prototype detector [25]. Besides the coaxial geometries, planar detectors with strip segmentation on both sides can be simulated too.

3. Results

In this section, we present the principle features of the signals from a highly segmented detector. The results of this investigation lead us to choose for the prototype ordered for MARS a segmentation with 6 sectors and 4 slices plus an additional segment on the front face; a $(6 \times 4 + 1)$-layout with 25 segments in total (Fig. 1).

Considering the planned application to extract positional information from the pulse shapes, the signals induced in the segments have to fulfil requirements in shape, amplitude and dynamic behaviour. The amplitudes have to be large enough to be well above the noise level, even for interactions depositing only small energies. Current charge preamplifier with a gain of about 100 mV/MeV have a noise level well below 1 mV. For a rough estimate, we consider a net charge signal originating from a small energy deposit of about 100 keV; a corresponding transient signal with an assumed relative amplitude of about 10% will have a signal-to-noise ratio smaller than 10. Hence, a requirement that useful transient signals should have, at least, relative amplitudes of about 10% is reasonable. Since the amplitudes of the transient signals depend mainly on the distance between the interaction point and the border to the sensing segment, as it will be demonstrated in the following subsections, this requirement limits the maximum size a segment can have. Besides the absolute amplitude, also the dynamic behaviour, i.e. the change of amplitude and shape, with respect to the positional coordinate of interest has to be examined; signals originating from interactions at different positions should be well distinguishable.

The response of a segment to an interaction, i.e. the signal induced in this segment, also changes with the position of the segment in the detector. In order to study the complete response of the detector, segments in the different parts of the detector are examined. For every examined segment, signals are calculated for a large number of interaction points covering its whole volume and, hence, resulting in a comprehensive characterisation of this segment. In Section 3.1, the signals from segments in the quasi-true-coaxial part of the detector are discussed. Approaching the closed-end cap of the detector, a difference between the geometrical and effective segmentation appears which will be addressed in Section 3.2.

The more complicated features of the signals from the segments in the closed-end cap will be presented in the following Section 3.3. Finally, the additional segment on the front face of the detector will be motivated in Section 3.4.

3.1. Segments in the quasi-true-coaxial part

The weighting potential applying high voltage to one segment in the quasi-true-coaxial part of the detector is shown in Fig. 2.

In order to investigate the behaviour of the signals as a function of the position, we calculated signals for points of interaction, as shown in Fig. 3. The coordinates z and φ are taken with respect to the centre of the segment at 0%, 25%, 50%, 75%, and 90% of half of the segment size (the total size of the segment is 2.5 cm in depth z and 60° in angle φ). For every pair (z, φ), the pulses are calculated for 8 equidistant radii between 0.55 and 3.7 cm (labelled A–H). In total, the set of 200 points covers one-quarter of the total volume of the segment (which represents the whole segment because of the coaxial symmetry).

In the quasi-true-coaxial part of the detector the hit segment, i.e. the geometrical segment in which the interaction took place, nearly always collects the net charge. Some of the signals of this segment as sensing segment are shown in Fig. 4. The total rise time of the signals depends only on the radial coordinate; in fact, it is the time the charge carriers need to reach their respective contact and, therefore, is determined by those charge carriers which arrive last. Moving the point of interaction from inner to outer radii (A $\rightarrow$ E), the total rise time of the signal decreases down to a minimum at an intermediate radius (E) where electrons and holes have approximately the same distance to reach their respective contact. From there the rise time increases again with increasing radial coordinates (E $\rightarrow$ H). Since the drift velocity is calculated using the real electric field inside of the detector with the full cylindrical symmetry, the total rise time does not depend on the angle φ. The electric field in longitudinal direction is only very small and, hence, has also no effect on the total drift time.

Since the individual shapes of the signals reflect the shape of the weighting potential, the influences of the segmentation are clearly visible. In order to present the entire response of the segment based on the set of 200 different pulse shapes, the main features are summarised in Fig. 5. To emphasise the influence due to the segmentation, the partial rise time T90 (i.e. the time from 10% to 90% of the maximum of the signal) instead of the total rise time is discussed. For each value of z (distinguished by different symbols) the weighted average over the 5 values of φ is plotted. The range of T90-values obtained for the 5 values φ is represented by the horizontal bar for each value z. The data points belonging to the same radial coordinate are connected by a line. For an unsegmented true-coaxial detector, these lines are straight perpendiculars and the horizontal bars vanish. It can be seen that, compared to the values at the centre of the segment, the averaged T90-times are shifted by up to 19% while the points of interaction approach the border to the neighbouring segment in longitudinal direction ($z = 0 \rightarrow 1.13$ cm). The variation around this average value due to the additional influence of the coordinate φ can be up to -20% and $+7\%$, respectively. The most sensitive points are around the radius F even for interactions in the centre of the segment far away from the border to the neighbours.

Points of interaction with different radial coordinates (e.g. radii B and H) can yield approximately equal partial rise times T90. However, since the signals have completely different shapes (Fig. 4) this ambiguity can be resolved, see Ref. [13].

The weighting potential outside the sensing segment is considerably smaller than inside; a longitudinal (top, right) and a horizontal (bottom, left) cut are shown in Fig. 2. Since the amplitudes of the transient signals reflect the magnitude of the weighting potential which the charge carriers traverse, their amplitudes are smaller than those of the corresponding net charge signals; at maximum they reach 40%. In Fig. 6, the transient signals from the angular neighbour of the hit segment are shown.

Since outside of the sensing segment the drift velocities of the charges can have any orientation

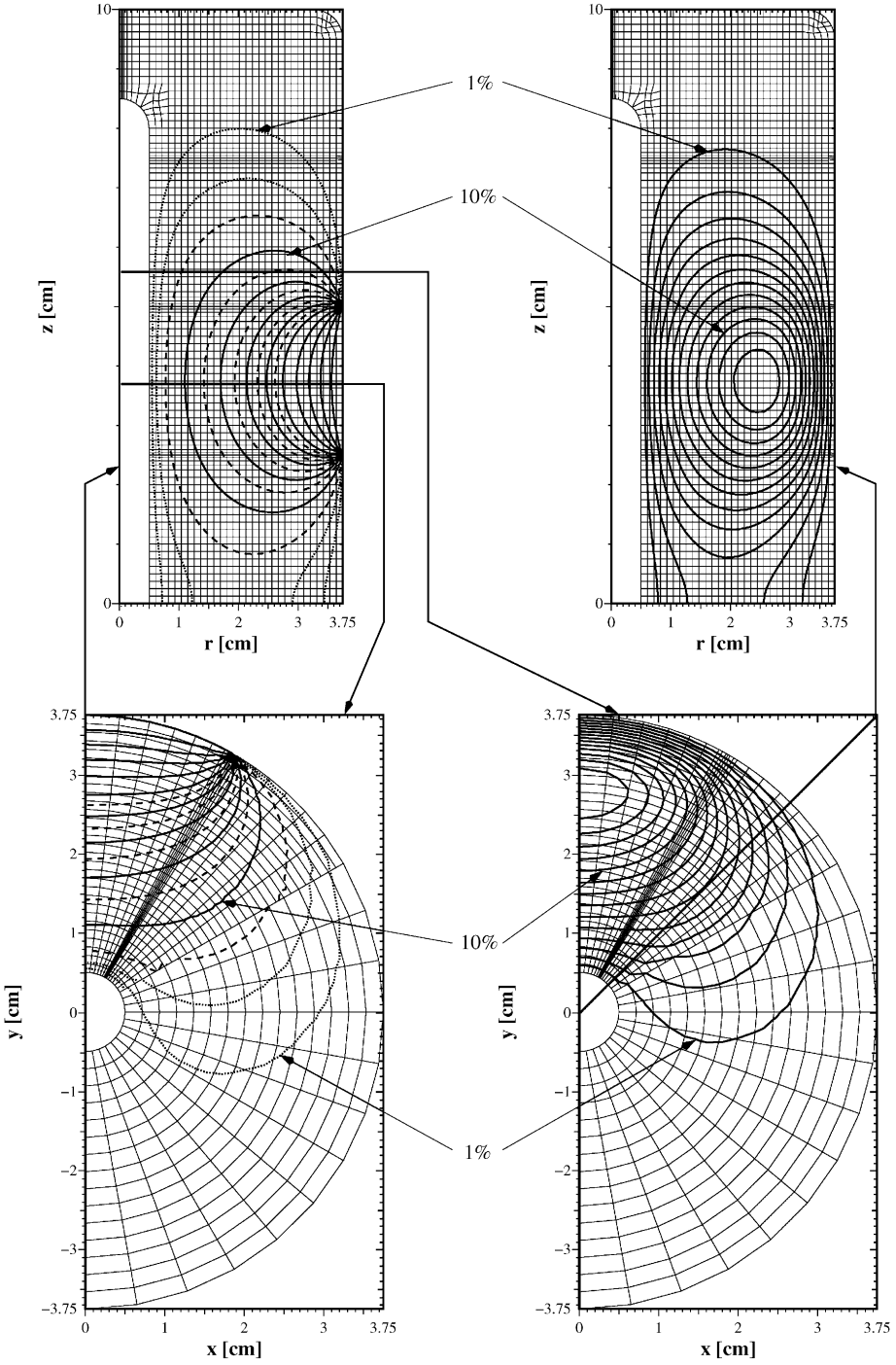

Fig. 2. Weighting potential of a sensing segment in the quasi-true-coaxial part of the detector (left). Equipotential lines are shown in steps of 10% of V_0 (solid), steps of 5% (dashed), and at 2.5% and 1% (dotted). Cuts through the adjacent sector (top, right) and the adjacent slice (bottom, right). Equipotential lines are shown in steps of 1% of V_0. The positions of the cuts are indicated.

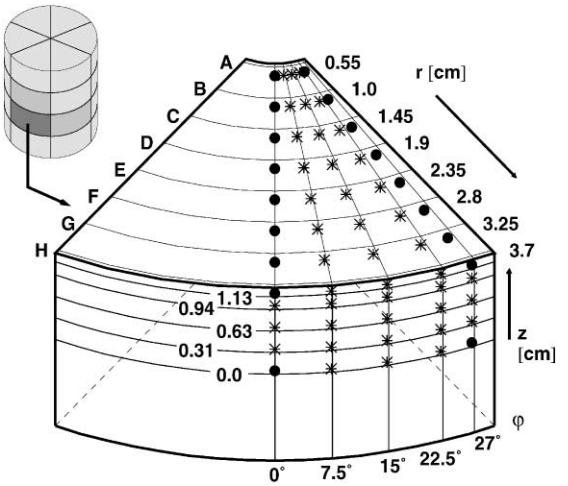

Fig. 3. Points of interaction within a segment in the quasi-true-coaxial part of the detector.

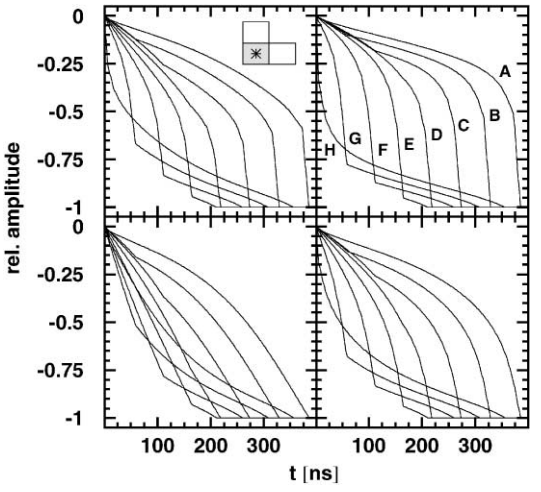

Fig. 4. Response of segments in the quasi-true-coaxial part of the detector: net charge signals for the points of interaction marked in Fig. 3 by a (●) which are the extremes of the area covered by the interaction points. The depths z are 1.13 (top) and 0.0 cm (bottom), the angles φ are 0° (left) and 27° (right). The sensing segment is highlighted, the hit segment is marked by a (∗).

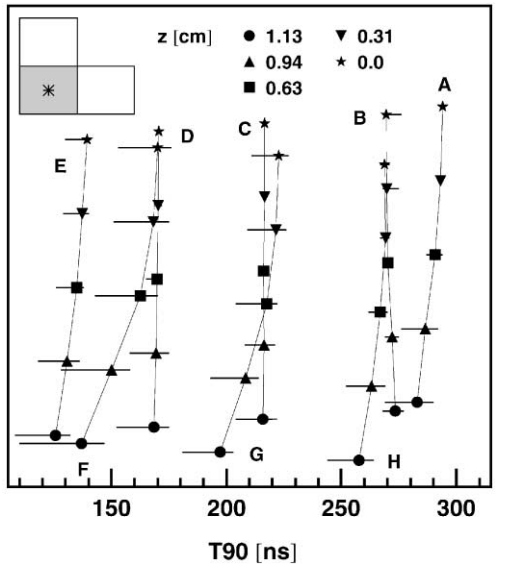

Fig. 5. Response of segments in the quasi-true-coaxial part of the detector: the characteristic curves of the partial rise times T90 for all points of interaction shown in Fig. 3; the data points are displaced arbitrarily in the vertical direction.

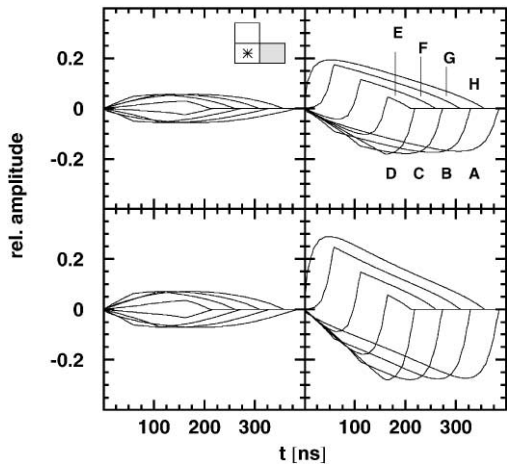

Fig. 6. Response of segments in the quasi-true-coaxial part of the detector: corresponding transient signals from the angular neighbour of the hit segment (same points of interaction like in Fig. 4).

with respect to the weighting field (Eq. (2)), transient signals are generally bipolar. Points of interaction at radii A–D induce negative signals dominated by the contribution from the holes which drift towards the outer contact traversing the maximum of the weighting potential (see upper right plot in Fig. 2). The electrons drift only a short distance towards the inner contact traversing a weaker weighting potential, therefore their contribution with opposite sign is outranged by that from the holes. Whereas for radii F–H, the

signals are dominated by the contribution from the electrons. Since in this case the orientation of the weighting field with respect to the drift velocity is the same as for the holes and the sign of the charge is reverse, the signals have positive maximal amplitudes. In fact, only the polarity of these transient signals can resolve the ambiguity in the correlation between T90 and r seen in Fig. 5. In case that the contributions from electrons and holes have similar amplitudes, they can add up to a wee or even vanishing sum signal, as it can be seen for interactions at radii of about half the distance between inner and outer radius, e.g. radius E, where the weighting potential has its maximum (see Fig. 2). From here both charges drift along a similarly shaped weighting potential towards the contacts. Both facts that the weighting potential is not completely symmetric with respect to its maximum and that the drift velocities are slightly different for electrons and holes result in a remaining signal.

In order to present the entire response of the segments also regarding the transient signals, their features are summarised in the following way: the characteristic curves shown in Fig. 7 are deduced from the maximum amplitude (positive or negative) and the time-to-maximum $T_{\max}$ of the transient signal for every pair (z, φ).

Since the transient signals from the angular neighbour of the hit segment mainly depend on the coordinate φ, it is reasonable to evaluate the signals by calculating for each value φ the weighted average over the 5 depths z. The bars represent the range of values caused by the less influential coordinate, i.e. the depth z, for each value φ. Points of interaction with the same radial coordinate are connected by a line which is then the characteristic curve shown in Fig. 7 (top). As the distance between the points of one curve is usually larger than the length of the bars, this form of representation of the signals is justified.

The transient signals from the longitudinal neighbour of the hit segment exhibit a similar behaviour, therefore they are presented in an analogous manner as characteristic curves in Fig. 7 (bottom). Since the more influential coordinate is here the depth z, the weighted average over the 5 angles φ is plotted for each value z. Again the bars show the effect of the less influential

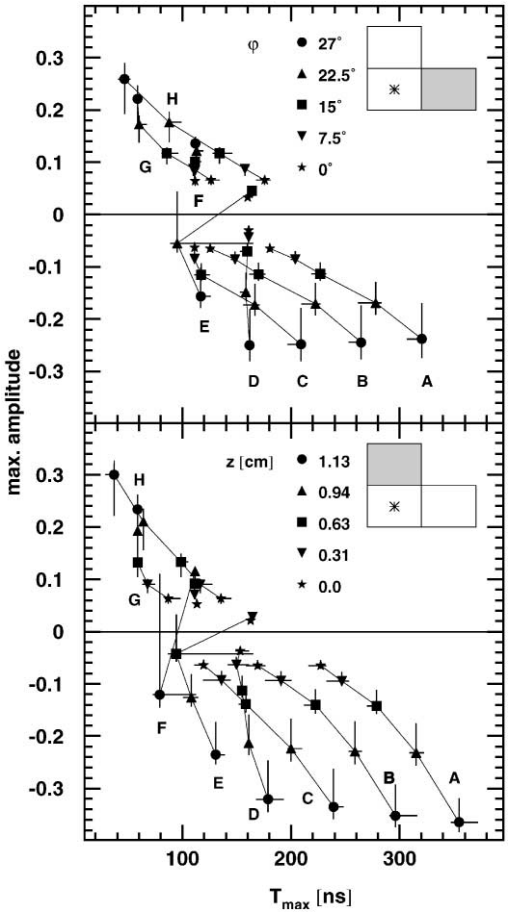

Fig. 7. Response of segments in the quasi-true-coaxial part of the detector: characteristic curves of the transient signals from the angular (top) and the longitudinal (bottom) neighbour of the hit segment (∗) for all points of interaction shown in Fig. 3.

coordinate, i.e. the angle φ, and the characteristic curve is the line connecting points with the same radial coordinate. The maximum amplitudes of the signals are slightly larger compared to those of the signals from the angular neighbour.

The distance between the data points of the characteristic curves is a measure for the dynamic behaviour, i.e. the sensitivity of the signals on the position. Better position determination can be expected, if the points are well separated and the bars are not overlapping. Except for the intermediate radial coordinates between D (1.9 cm) and F (2.8 cm), these conditions are fulfilled. It can be noted also that for most parts of the segment

the amplitudes of the transient signals are larger than the 10% limit. Points of interaction close to the centre of the hit segment result in small transient signals in the neighbouring segments and it is clear that they vanish eventually for points even further away from the relevant sensing segment. Since the maximum amplitude can change from a positive to a negative extremum or vice versa, the bipolar signals at the intermediate radial coordinates are anyway not very well represented in this simplified scheme: the large bars indicate more significant changes in shape than they actually are. However, the amplitudes of the transient signals for intermediate radii tend to be smaller than for smaller or larger radii, as it was mentioned already before. Hence, a worse position determination can be expected at these radii.

From this analysis we can conclude that the gross shape of the net charge signals as well as the transient signals depends mainly on the radial coordinate of the point of interaction. The dependence of the shape on the depth z and the azimuthal angle φ is less pronounced. On the other side, the amplitudes of the transient signals vary predominantly with the distance to the border between the sensing segment and the segment collecting the net charge, i.e. with z for the longitudinal neighbour or φ for the angular neighbour; they are affected only weakly by the second coordinate φ or z, respectively. The dependence of the amplitude on the radial coordinate r is only very smooth, except for a range of intermediate radial coordinates where the maximum changes sign. In the quasi-true-coaxial part of the detector, a simple scheme for position determination can be established: the radial coordinate can be deduced from the net charge signal of the hit segment; then the amplitudes of the transient signals from the neighbouring segments determine the other two coordinates z and φ. In the following subsections it will be demonstrated that such a simple one-dimensional method is not adequate for the closed-end cap of the detector.

3.2. Segments near to the closed-end cap

Compared to the segments in the quasi-true-coaxial part discussed in the previous subsection, the response of a segment of the slice above shows already significant changes caused by the electric influence of the closed-end cap.

Placing the points of interaction at the same relative positions like in Fig. 3 within this segment, the corresponding characteristic curves are shown in Figs. 8 and 10.

The partial rise times T90 are not much changed. Depending on the depth z, their average values can be shifted by up to 13%. The influence of the angle φ causes a variation of up to -19% and $+6\%$, respectively.

Most obvious difference is the fact that the hit segment, i.e. the geometrical segment which accommodates the interaction, does not always collect the net charge! The longitudinal drift due to the longitudinal component of the electric field can be sufficient that the holes cross the border to the segment of the front slice which then collects the net charge. In Fig. 8, the corresponding data points are also plotted in the diagram as solitary points or points connected by a dashed line (dotted lines merge the points belonging to one radial

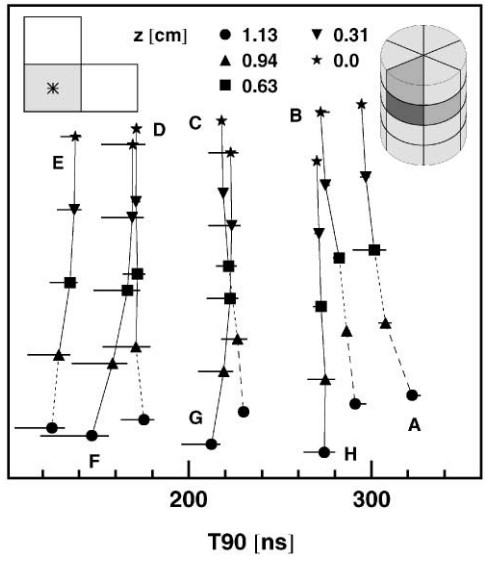

Fig. 8. Response of segments near to the closed-end cap (points of interaction distributed like in Fig. 3): the characteristic curves of the partial rise times T90. For solitary points and points connected by a dashed line, the longitudinal neighbour collects the net charge (both groups of points are merged by dotted lines to guide the eyes).

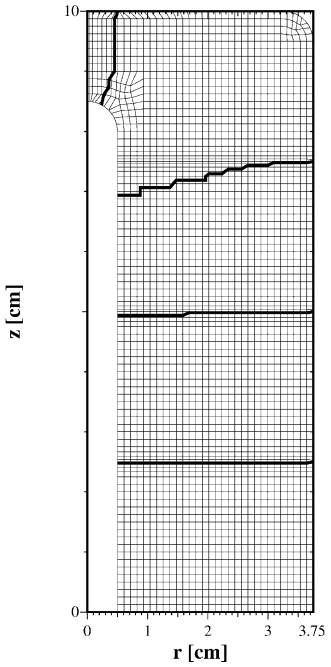

Fig. 9. Calculated shape of the effective segments (the additional front segment with a radius of 5 mm, addressed in Section 3.4, is already included).

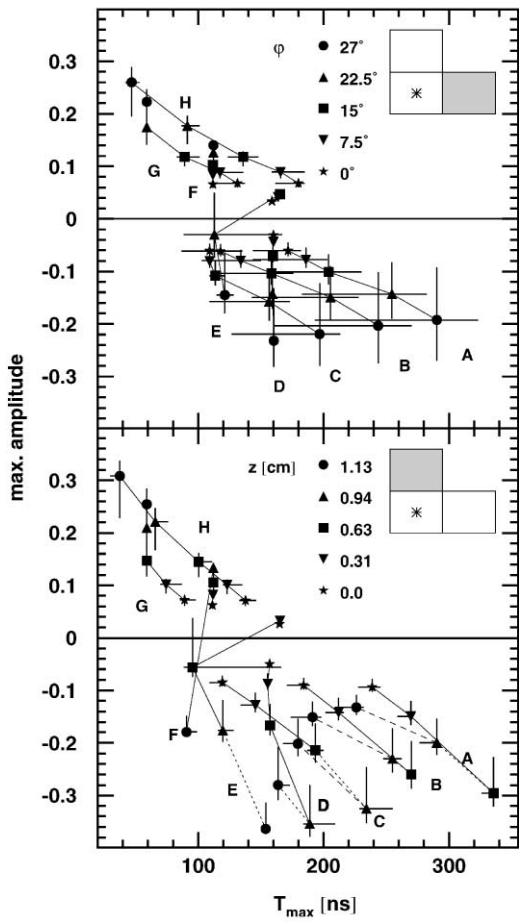

Fig. 10. Response of segments near to the closed-end cap: characteristic curves of the transient signals of the angular (top) and longitudinal (bottom) neighbour of the segment shown in Fig. 8 (same points of interaction).

coordinate to guide the eyes). For the small radii, A–C, points of interaction which are closer than at least 0.3 cm ($z \geqslant 0.94$ cm) to the border of the segment induce the net charge signal in the segment above. For the larger radii D and E, interaction points in the direct vicinity of the border between the two slices still show this behaviour. However, the dependence of the rise time T90 on the radius does not change significantly as the segment which collects the net charge changes indicating that the influence of the depth z on the shape of the signal is still moderate. Finally, it has to be noted that also the variation of the total rise time of the signals for a specific radius as a function of the depth z is still small, in the order of a few ns.

In contrast to the geometrical segments, we have now to consider effective segments defined as the volume which accommodates the points of interaction whose net charge is collected on the outer surface by the contact of this specific segment. As shown in Fig. 9, we deduced the borders of these effective segments by determining the contact which collects the net charge for interactions at every node of the grid. In fact, it can be seen that at small radii $r \leqslant 0.9$ cm the effective segment in the front slice extends up to 0.56 cm ($\approx 22\%$ of the total segment size in depth) into the geometrical segment below.

The signals from the angular neighbour exhibit for the inner radii A–D an increased influence of the depth z represented by the bigger horizontal and vertical bars, compare Figs. 7 and 10 (top).

The signals from the longitudinal neighbour are not affected for the outer radii E–H, but the

amplitudes are up to a factor of 2 larger for the smaller radii A–D, as it can be seen from a comparison between Figs. 7 and 10 (bottom).

Analogous to Fig. 8, the solitary points and the points connected by a dashed line are derived from transient signals from the hit segment. These additional points fit quite well to the characteristic curves determined for the longitudinal neighbour. The maximum amplitude increases for increasing radii (A → E) at a depth $z = 1.13$ cm indicating a decreasing distance to the borderline. On the other hand, the amplitudes decrease for the same radii at a depth $z = 0.63$ cm indicating an increasing distance to the borderline. This effect is a clear evidence that the distance to the border between the effective segments is the significant parameter and the signals are symmetric with respect to this borderline.

3.3. Segments in the closed-end cap

Already in the previous subsection became evident that the closed-end cap differs significantly from the quasi-true-coaxial part of the detector. In Fig. 11, the weighting potential is shown applying high voltage to one segment of the front slice of the detector.

Since the main change is the increasing importance of the depth z, the points of interaction now have to span the total longitudinal length of the segment, which is done in equidistant steps of 0.5 cm, as it can be seen in Fig. 12.

In Fig. 13, some of the net charge signals are shown (the point at radius H and depth $z = 1.0$ cm is outside of the detector volume because of the bulletised edge of the front face). It has to be stressed that the signals are not grouped anymore with respect to the radial coordinate. This becomes even more obvious presenting the signals as characteristic curves of the partial rise time T90, which are shown in Fig. 14. Near to the border to the segment below ($z = -1$ cm) the characteristic curves are similar to those of that segment, as it can be seen in comparison with Fig. 8. Beginning with points of interaction at small radii A–C, the behaviour changes as soon as the points of interaction are at larger distance to that border. Eventually, the partial rise time exhibits a completely different but very regular behaviour: in the second half of the front slice ($z > 0$ cm), the dependence of T90 on the radius r is nearly linear. While the symmetry of the T90 values with respect to the intermediate radius E mentioned in Section 3.1 still remains near to border to the segment below ($z = -1$ cm), it is evident from the diagram that new ambiguities appear. The T90 values originating from points of interaction at small radii A and B span as function of the depth z the whole range of values for T90. At larger radii (C–H) and depths $z \geqslant 0$ cm, the same T90 values can be obtained for different combinations r and z, e.g. (D, $z = 1.0$ cm), (E, $z = 0.5$ cm), and (F, $z = 0$ cm).

Also the transient signals from the angular neighbour, shown in Fig. 15, depend strongly on the depth z. Compared to the situation in the quasi-true-coaxial part presented in Fig. 6, a remarkable difference is that the signals for the radii A–D as a function of z yet change polarity. Therefore, summarising their main features in form of characteristic curves based on values averaged over z is not reasonable anymore. In Fig. 16 (top), for each value z the individual data points for the 5 angles φ are plotted and connected by a line defining a new type of characteristic curve. The figure shows the respective characteristic curves for two different radii, B and G. It is evident that the dependence on the angle φ is outranged by that on the depth z. The correlation between increasing amplitudes of the signals from the angular neighbour and decreasing distance of the interaction point to the border to that segment is, of course, still existent. On the other hand, ambiguities in the correlation between pairs (r, z) and partial rise times T90 can be resolved partially by analysing the signals from this angular neighbour.

Regarding the longitudinal neighbour, which is for a segment of the front slice the segment below, only limited information can be obtained from the characteristic curves shown in Fig. 16 (bottom). The amplitudes are only for a few points larger than 10% and not well separated. Since the points of interaction cover the whole volume of the segment, a comparison to the characteristic curves shown in the previous subsections has to notice the

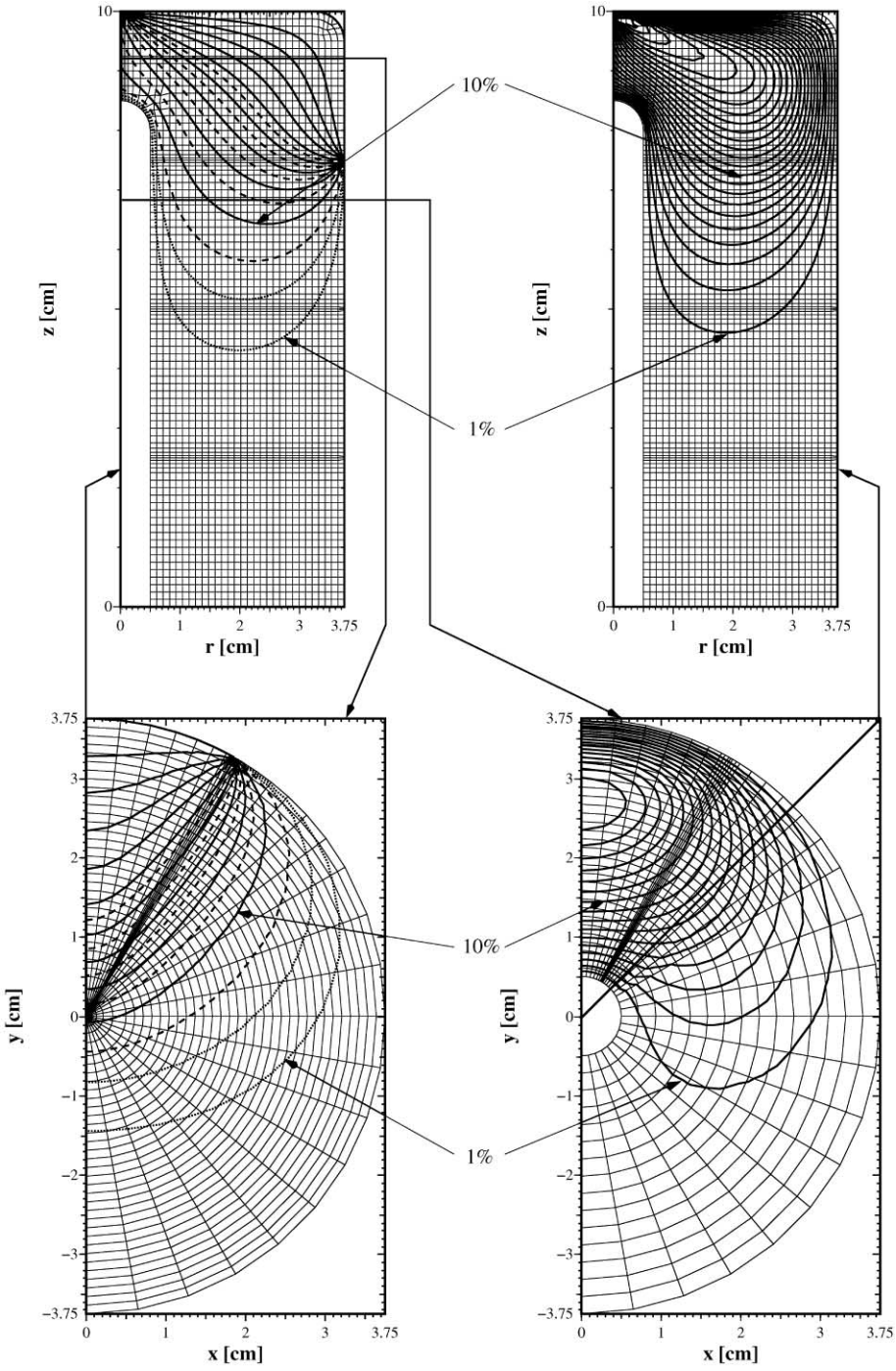

Fig. 11. Weighting potential of a sensing segment in the closed-end cap. Cuts through the adjacent sector (top, right) and the adjacent slice (bottom, right). The positions of the cuts are indicated. Equipotential lines like in Fig. 2.

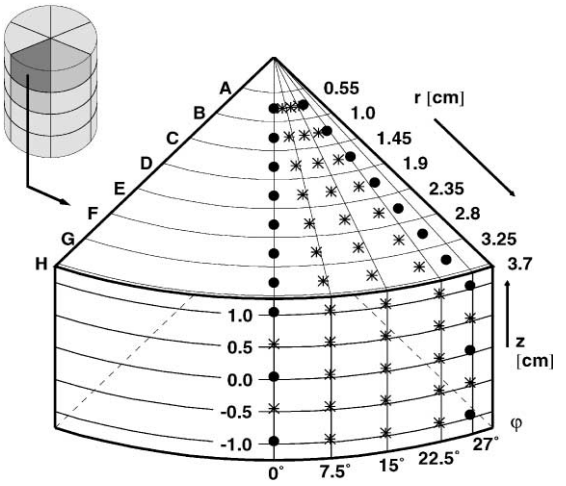

Fig. 12. Points of interaction within a segment in the front slice of the detector.

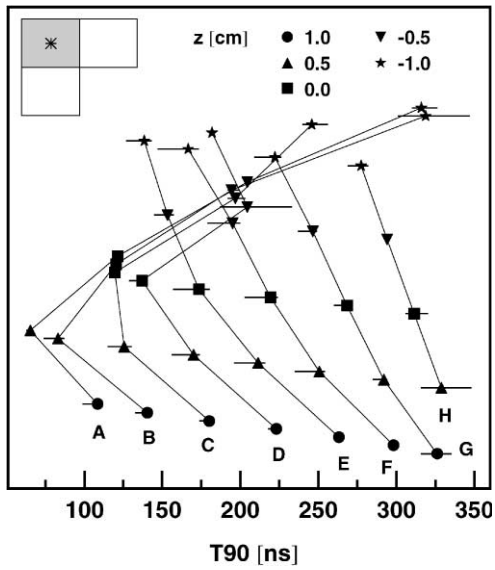

Fig. 14. Response of segments in the front slice of the detector: the characteristic curves of the partial rise times T90 for all points of interaction shown in Fig. 12.

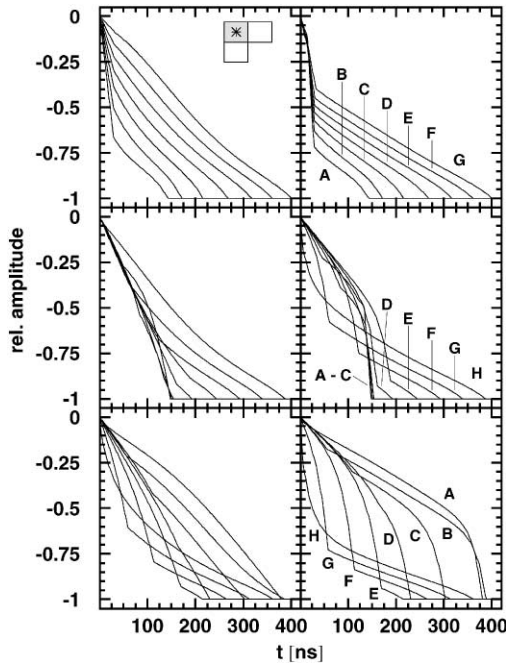

Fig. 13. Response of segments in the front slice of the detector: net charge signals for the points of interaction marked in Fig. 12 by a (●). The depths z are 1.0 (top), 0.0 (middle), and −1.0 cm (bottom), the angles φ are 0° (left) and 27° (right). The sensing segment is highlighted, the segment which accommodates the interactions is marked by a (∗).

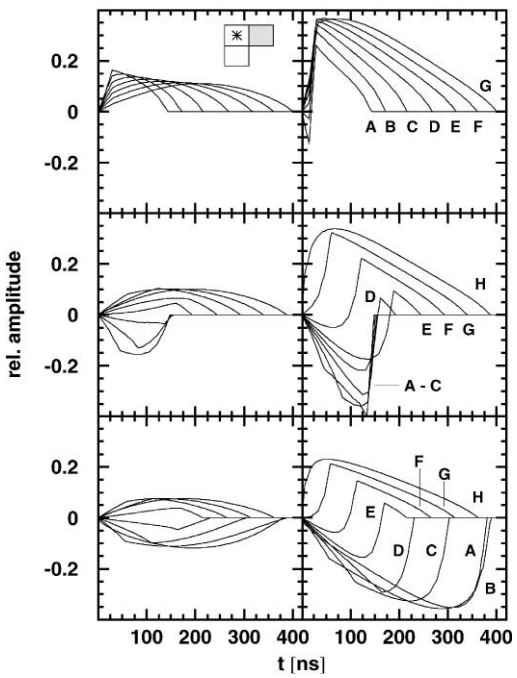

Fig. 15. Response of segments in the front slice of the detector: corresponding transient signals from the angular neighbour of the hit segment (same points of interaction like in Fig. 13).

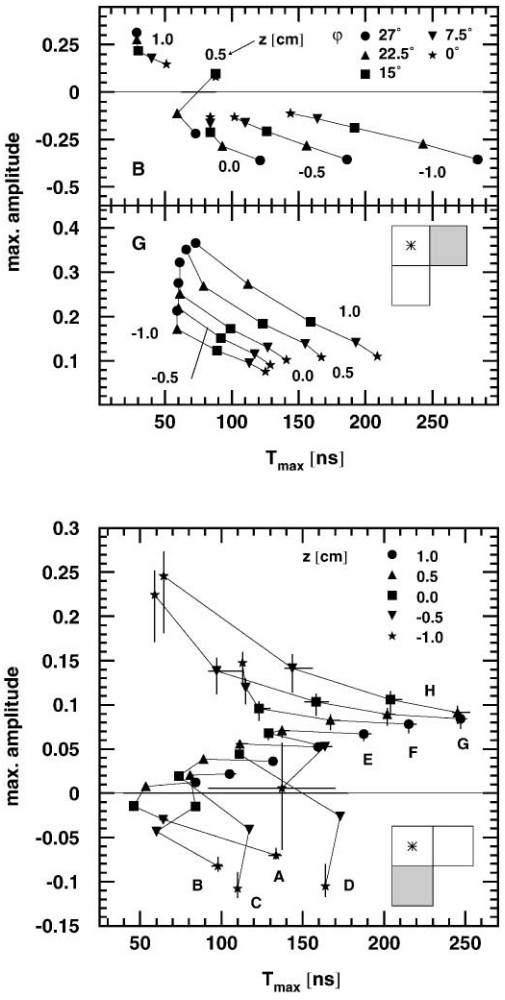

Fig. 16. Response of segments in the front slice of the detector: characteristic curves of the transient signals from the angular (top) and longitudinal (bottom) neighbour of the hit segment shown in Fig. 13 (same points of interaction): (Note: the characteristic curves of the angular neighbour (top) are plotted only for two different radii B and G, see text).

partly larger distances to the segment border. However, for the determination of the depth z within segments of the front slice the signals from the longitudinal neighbour below are of less importance since its own signals contain already much information about the depth itself.

We can conclude that the response of a segment in the front slice of the detector is explicitly different from the other segments, as it can be expected from the completely different geometry. In particular, all signals depend to a similar extent on the radius r and the depth z. The basic requirements for pulse shape analysis are fulfilled, the dynamic behaviour is even more pronounced, but the correlation between pulse shape and position of the interaction is much more complicated. Consequently, the simple method to determine the position of the interaction points that was applicable for the quasi-true-coaxial part of the detector (Section 3.1) clearly has to be replaced by a more refined analysis taking this into account.

3.4. Segment on the front face of the detector

The central part of the closed-end cap, i.e. the zone in front of the inner hole, is usually considered to be a quasi-planar detector. This is established by the fact that, for a detector without angular segmentation, the potential in this zone depends only smoothly on the radius and almost linearly on the depth (see e.g. Ref. [13]). Although the weighting potentials of a detector with angular segments exhibit these features to a smaller extent, as it can be seen in Fig. 11, it can be expected that still the achievable resolution for the radial coordinate r is worse and the determination of the depth z is ambiguous. Since this zone is far away from the slice below, the tiny transient signals induced there are not helpful, as it can be seen for radii A–D and depths $z \geqslant -0.5$ cm in Fig. 16 (bottom).

Aiming to obtain further information for an improved position determination in this particular zone, we added an additional segment on the front face of the detector. The signals, net charge as well as transient signals, from this front segment are especially sensitive on points of interaction in the central part of the closed-end cap and, therefore, provide additional positional information. This will be targeted more detailed in the following.

In Fig. 17, the weighting potentials in the closed-end cap of the detector are shown whereby successively an additional front segment with a radius of 2.5, 5, and 10 mm is considered. As it was discussed already previously, useful transient signals principally can be expected from a zone where the charge carriers traverse a weighting

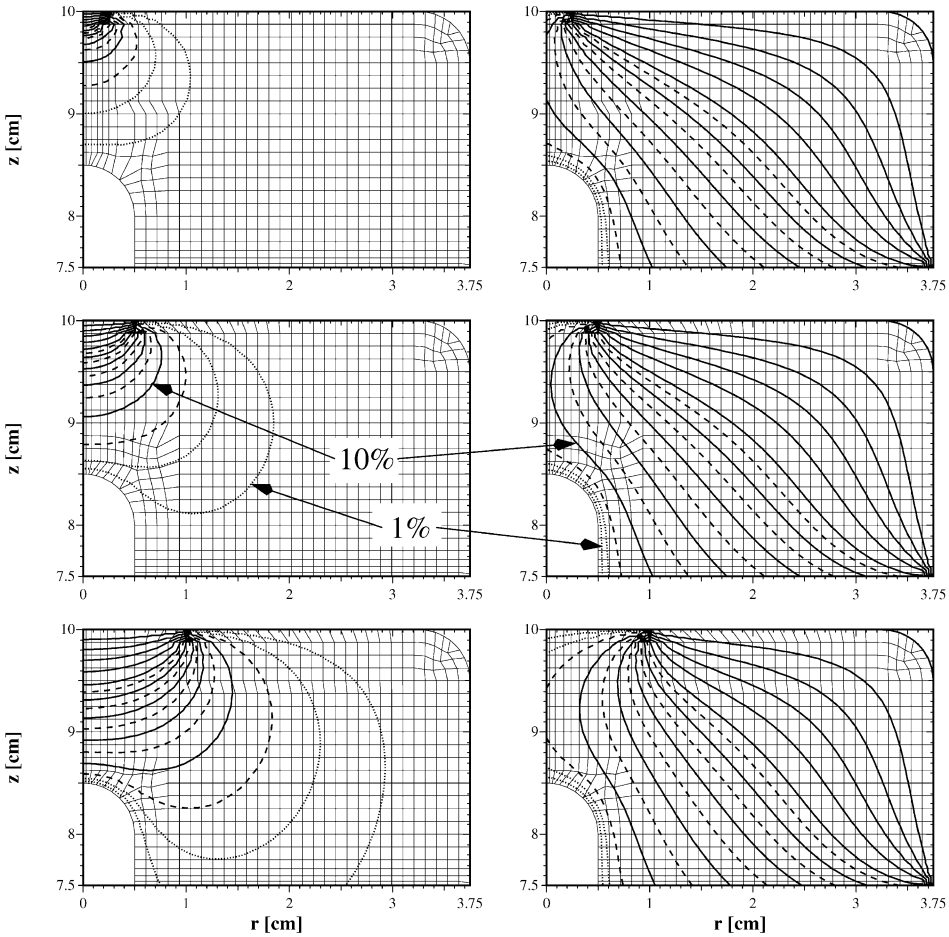

Fig. 17. Weighting potentials in the closed-end cap of the detector with an additional front segment with a radius of 2.5 (top), 5 (middle), or 10 mm (bottom). The sensing segment is the front segment (left) or the neighbouring sector (right); the cuts are through the centre of the segment. Equipotential lines like in Fig. 2.

potential with a maximum value of at least 10% of the applied bias and, hence, can induce signals with corresponding amplitudes. It can be seen in the figure that the size of this zone depends, of course, on the radius of the front segment.

The subsequent discussion of the features of the signals is based on points of interaction which are distributed within the central part of the closed-end cap in the following manner (Fig. 18): the angle φ is varied like in the preceding subsections; the depth z varies between 8.6 and 9.9 cm in 5 equidistant steps covering the distance between the end of the inner hole ($z = 8.5$ cm) and the front face ($z = 10$ cm); and the 8 radial coordinates are 0.1, 0.2, 0.3, 0.4, 0.6, 0.8, 1.1, and 1.5 cm, labelled A–H.

Fig. 19 shows some signals from the segments in the front slice assuming a front segment with a radius of 5 mm. Depending on radial coordinate and depth either the front segment or the adjacent sector collects the net charge. The corresponding characteristic curves are shown in Figs. 20 and 21. As we have already demonstrated, in the closed-end cap the depth z is more important than the angle φ, hence the data points of the characteristic curves are calculated for each value z by taking the weighted average over the 5 angles φ. According to the cylindrical symmetry of the front segment, its

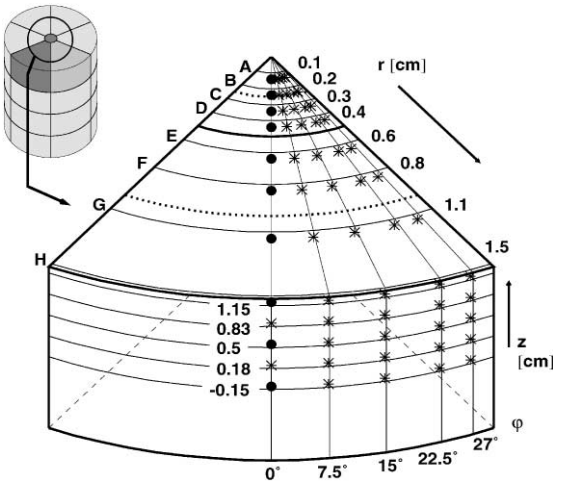

Fig. 18. Points of interaction within the central part of front slice of the detector ($r \leqslant 1.5$ cm). The additional front segment with a radius of 5 mm is indicated with a solid line, those with radii 2.5 and 10 mm with dotted lines.

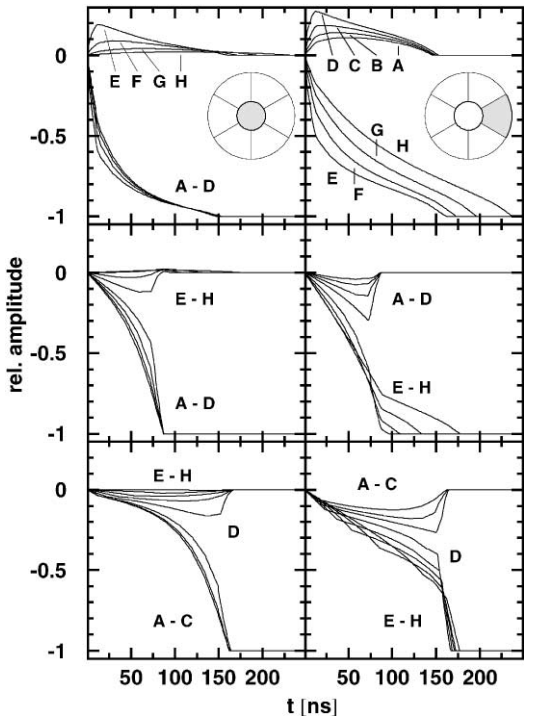

Fig. 19. Response of the central part of the front slice: signals from the front segment with a radius of 5 mm (left) and the neighbouring sector (right) for the points of interaction marked in Fig. 18 by a (●). The depths z are 1.15 (top), 0.5 (middle), and −0.15 cm (bottom), all at an angle φ of 0°.

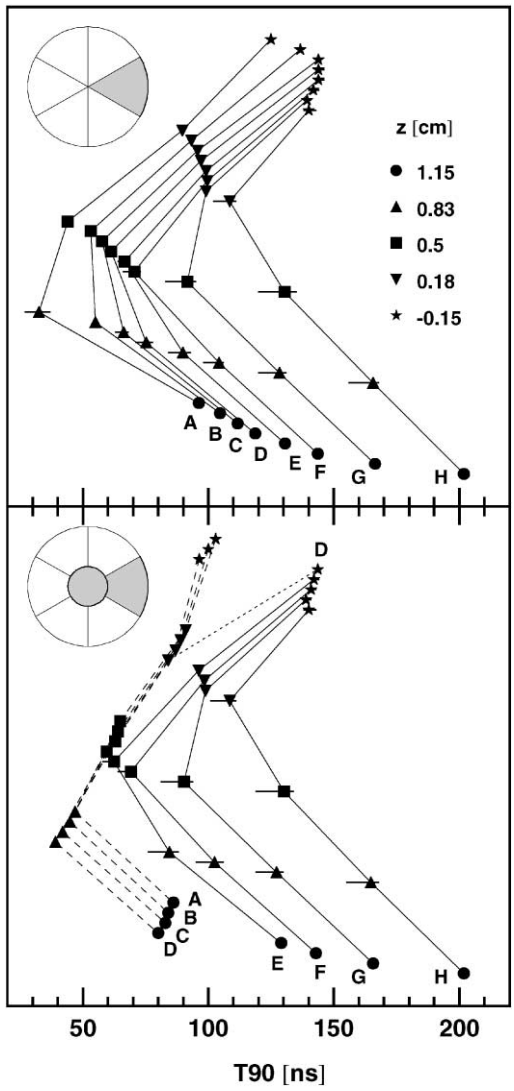

Fig. 20. Response of the central part of the front slice: the characteristic curves of net charge signals from a detector without (top) and with additional front segment (bottom) for the points of interaction shown in Fig. 18. Data points from the front segment are connected by dashed lines, those for the adjacent sector by solid lines, the dotted line is to guide the eyes (see text).

net charge as well as transient signals are, as a matter of principle, independent of the angle φ; therefore the bars indicating the influence of this angle always vanish.

Regarding the net charge signals, in Fig. 20 the characteristic curves of the rise times T90 are

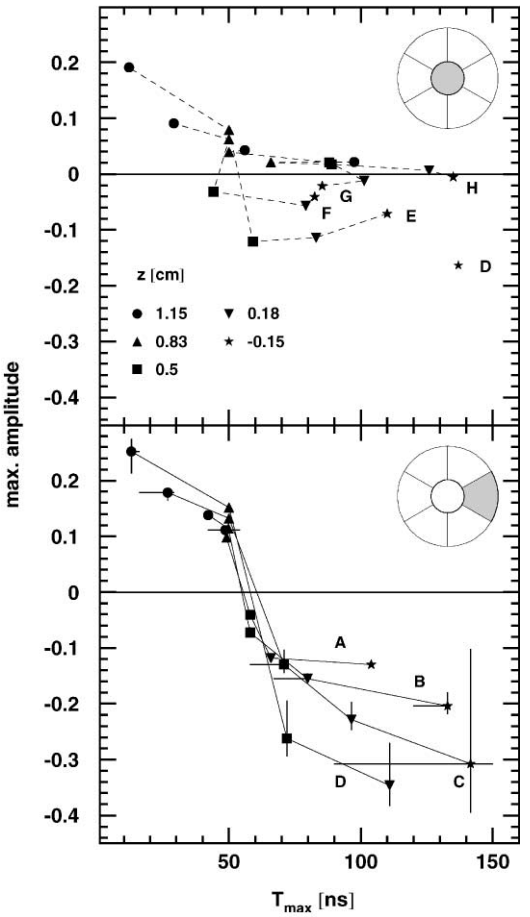

Fig. 21. Response of the central part of the front slice: characteristic curves of the transient signals corresponding to the net charge signals shown in Fig. 20 (bottom). The sensing segment is highlighted.

shown. In order to expose the effect of the front segment, these curves are compared to the corresponding ones for a detector without this additional segment. Leaving out the front segment, only a smooth dependence on the radial coordinate exists for interactions at radii A–F (as a remark, the upper part of Fig. 20 is a refined view of the lower left corner of Fig. 14). If the front segment is added, it collects the net charge of interaction points at radial coordinates A–D. Showing no dependence on the radial coordinate, these curves are even more similar to those from a planar detector.

In a planar detector the electric field is constant resulting in a linear dependence of the rise time on the depth z. Starting from the half distance between inner and outer contact, both charge carriers have the same distance to drift and the total rise time of the induced signal is minimal. If the point of interaction is closer to one of the contacts, the charge carriers which are farther away from their collecting electrode govern the total rise time. Hence, the rise times exhibit a symmetry with respect to this point of half distance between the contacts (neglecting for this simple discussion the different drift velocities of electrons and holes). However, this symmetry is not apparent completely yet (Fig. 20, bottom).

For points of interaction at larger radial coordinates (E–H), the net charge is collected by the adjacent sector. The signals remain nearly unaffected by the additional front segment. The solitary data point at (D, $z = -0.15$ cm) evidences that geometrical and effective segmentation differ also in this zone of the detector. The radial drift caused by the radial component of the electric field is sufficient for the holes to cross the border to the adjacent sector which then collects the net charge. Fig. 9 shows the effective size of the front segment with a radius of 5 mm.

In Fig. 21, the characteristic curves of the corresponding transient signals are shown. For interactions at large radial coordinates (E–H), the transient signals from the front segment generally are very small and the curves are not very well separated, therefore these signals will not provide much further information for position determination (Fig. 21, top). For smaller radii (A–D), the characteristic curves of the transient signals from the adjacent sector are shown in Fig. 21 (bottom). With increasing radial coordinate the amplitudes become larger and, in particular near to the end of the inner hole ($z \leqslant 0.18$ cm), the curves are well separated so that the different radial coordinates can be distinguished. However, for intermediate values of z the points of the different curves cannot be disentangled. In any case, the ambiguity in the correlation between the rise time T90 and the depth z can already be resolved by just the sign of the transient signal from the front segment.

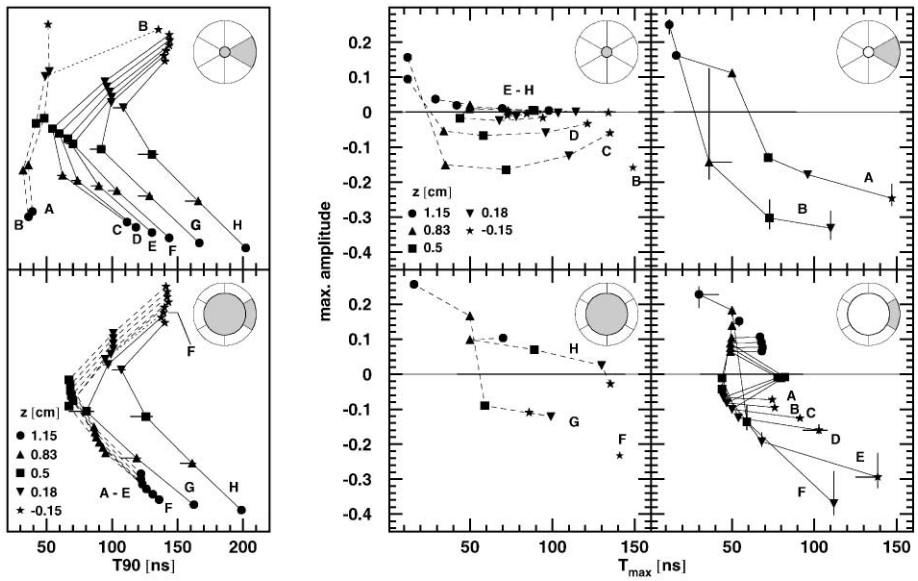

Fig. 22. Response of the central part of the front slice: the characteristic curves of net charge signals (left) and transient signals (middle and right) assuming a front segment with a radius of 2.5 (top) and 10 mm (bottom). Same symbols and points of interaction like in Fig. 20.

In order to investigate the effects of an additional segment on the front face more deeply, in Fig. 22 characteristic curves are represented assuming a smaller and a larger front segment with radii of 2.5 and 10 mm, respectively. Both the characteristic curves of the net charge signals (left) and the transient signals (middle and right) are shown.

Considering a smaller front segment with a radius of 2.5 mm (Fig. 22, top), the net charge signals originating from interactions at radial coordinates larger than 0.2 cm (C–H) are collected by the adjacent sector. The characteristic curves of these signals are nearly the same like for a detector without a front segment and, consequently, the corresponding transient signals from the front segment are small. Except for radius C which is in the direct vicinity of the border between the relevant segments, these signals are hardly useful. For smaller radial coordinates, A and B, the front segment collects the net charge. The rise times T90 are independent of both the radial coordinate and the depth, but large and well separated transient signals in the adjacent sector resolve the ambiguities. Unfortunately, this is valid only for the few interactions within a very limited volume, in accordance with the small extension of the weighting potential of the front segment, as shown in Fig. 17. Since additional information is desired from a larger zone than this, i.e. for radial coordinates up to D or E, a useful front segment has to have a larger dimension.

The opposite can be deduced considering a larger front segment with a radius of 10 mm (Fig. 22, bottom). Only for the large radial coordinates G and H, the adjacent sector collects the net charge signal. The characteristic curves of the partial rise times T90 exhibit ambiguities which can be resolved analysing the corresponding transient signals from the front segment. For interaction points at smaller radial coordinates (A–E), the front segment collects the net charge and the characteristic curves of the rise times T90 are nearly perfectly those of a planar detector: no dependence on the radius and rise times T90 symmetric with respect to the half distance between inner contact and front face ($z = 0.5$ cm). Except for points of interaction near to end of the inner hole ($z = -0.15$ cm), the characteristic curves of corresponding transient

signals from the adjacent sector offer hardly additional information. Obviously, adding a large front segment even worsens the capability for position determination in the central part of the closed-end cap of the detector.

In both cases, solitary data points in the plots of the characteristic curves indicate that the holes have crossed the border between the segments, hence the hit segment does not collect the net charge.

It is clear that the segment on the front face of the detector with its cylindrical symmetry worsens the determination of the angular coordinate φ. In order to investigate this effect, in Fig. 23 the transient signals from the angular neighbour are presented assuming a front segment with different radii. As discussed in the previous subsection, it is not reasonable to discuss the dependence on the angle φ averaged over the depth z, therefore characteristic curves for interactions with radial coordinates B ($r = 0.2$ cm) and E ($r = 0.6$ cm) are plotted for each value z separately.

For points of interaction at the small radial coordinate B (left column in the figure), the characteristic curves are more and more compressed with increasing radius of the front segment (from top to bottom) and, eventually, collapse completely. Also the interaction points at the larger radial coordinate E (right column in the figure) exhibit a similar behaviour: the

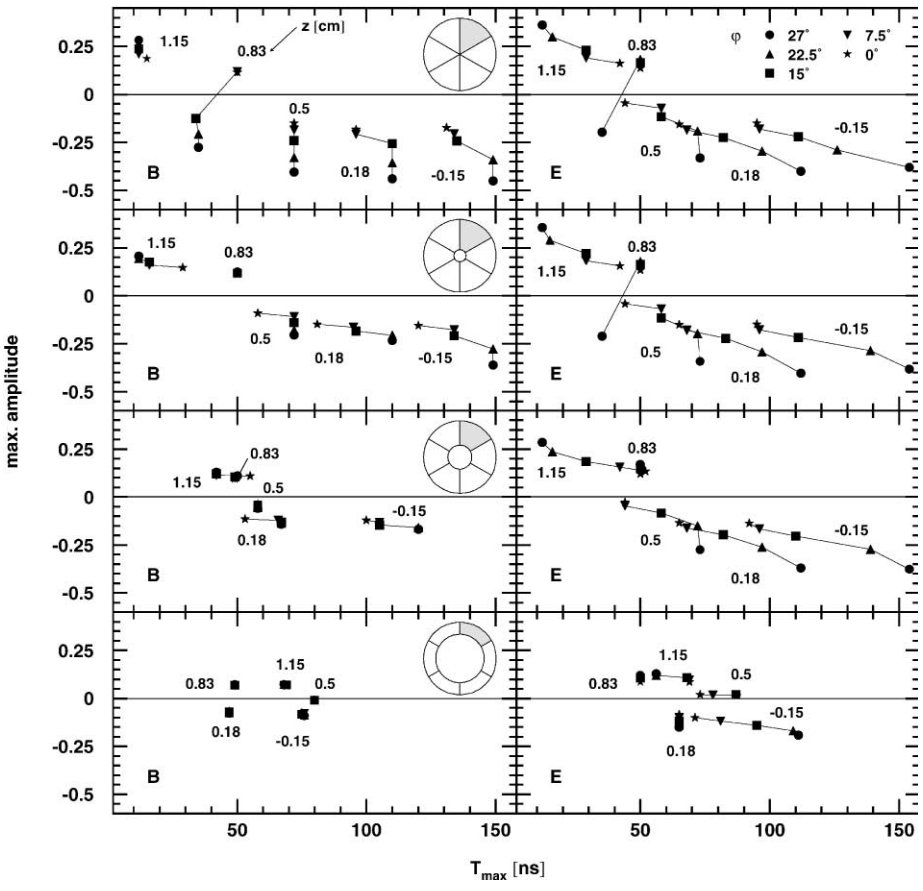

Fig. 23. Response of the central part of the front slice: the characteristic curves of transient signals in the angular neighbour (highlighted) assuming no front segment, a front segment with a radius of 2.5, 5, and 10 mm (from top to bottom) calculated for interaction points at the radial coordinates B and E (see text).

characteristic curves remain mainly undisturbed as long as the radius of the front segment is smaller than this radial coordinate or else the angular information is lost. Comparing the two columns, it is obvious that the angular coordinate φ of an interaction point cannot be determined anymore if its radial coordinate undercuts the radius of the front segment by more than roughly 1 mm.

Aiming at the determination of the three-dimensional position, the angle φ is less important for small radial coordinates (e.g. radius B), but at larger radii (e.g. radius E) the lack of the angular coordinate is not acceptable. Since the analysis of any other signal cannot recover the loss of information about the angular position, a front segment with a radius larger than some mm has to be ruled out.

It can be concluded that an additional segment with a radius of 5 mm on the front face of the detector is a reasonable compromise, offering valuable information to resolve the ambiguities in the position determination originating from the quasi-planar detector in the central part of the closed-end cap. Smaller front segments are useful only in a region of insufficient size whereas larger front segments even increase the problems caused by the quasi-planar zone. From the results presented in this subsection, we decided to add to the prototype detector ordered for MARS a front segment with a radius of 5 mm, which is anyway the minimum radius required by the manufacturer to place an electrical contact on the segment.

4. Conclusion and outlook

A crucial step on the way to a γ-ray tracking array is the position determination of the points of interaction. This determination has to be done within a resolution of a few mm, in order to allow to track the scattering path of each γ-ray. This position resolution can be obtained by a combination of two-dimensional electrical segmentation of the detector and pulse shape analysis. In order to investigate the influence of the size and the arrangement of the segments as well as the shape of the crystal, we developed programs to simulate the signals for detectors of various geometries.

Since the desired position resolution is in the range of some mm, the response of the detector has to be studied in a very detailed way taking into account carefully the differences between the parts of the detector. In order to obtain the comprehensive response of the detector to single interactions, we studied the individual response of sensing segments, i.e. the signals from these segments, in all parts of the detector for a large set of points of interaction.

In Section 3, we have presented simulated pulse shapes from a large cylindrical n-type HPGe detector with closed-end geometry and a $(6 \times 4 + 1)$-layout of the segments. The shapes of calculated signals were discussed introducing simplified characteristic curves representing the most important features of the signals. Generally, there are two types of signals: net charge signals if the sensing segment collects the charge produced by an interaction; or, if one of the neighbouring segments acts as sensing segment, transient signals which have eventually a zero net charge. A position determination only based on net charge signals is not sufficient for γ-tracking, a more accurate result can be achieved by analysing also these transient signals.

In Section 3.1, segments in the quasi-true-coaxial part of the detector were discussed. The signals, both net charge and transient, exhibit as gross characteristics that the shape depends predominantly on the radial coordinate of the interaction point. The amplitudes of the transient signals are a measure of the distance between the interaction point and the border to the sensing segment. This information can be applied to determine the depth z and the azimuthal angle φ in a rather straightforward way.

The influence of the closed-end cap of the detector on the signals is considerable, already 2 cm before the end of the inner hole, geometrically the subdivision between the quasi-true-coaxial part and the front cap, as it was demonstrated in Section 3.2. Most striking effect is the emerging difference between geometrical and effective segmentation: the hit segment, i.e. the geometrical segment which accommodates the point of

interaction, does not necessarily also collect the generated charge; and the transient signals vary with respect to the distance to the borderline between these effective segments. It is indubitable that this effect becomes even more important for detectors having more (and thus smaller) slices, in particular for slices in the first few cm of the detector, like for the GRETA prototype detector [25].

In Section 3.3, segments in the closed-end cap were discussed. The pulse shapes show a much more complicated behaviour. In particular, the dependence of the gross shape on the depth and on the radial coordinate are of equal importance, hence a simple classification of the shapes only in terms of the radial coordinate is not possible anymore, the analysis has to be more detailed.

The additional segment on the front face of the detector was discussed in Section 3.4. In front of the end of the inner hole, the quasi-planar geometry causes ambiguities in the determination of the radial coordinate and the depth. These can be resolved by adding a further segment on the front face. The effects of such a cylindrically symmetric segment on the signals have been discussed in detail concluding that a segment with a radius of 5 mm will offer valuable information from this area. It has to be noted that also for such a front segment, geometrical and effective segmentation differ, as shown in Fig. 9.

From the examination of the response of the different parts of the detector presented in Section 3, we can conclude that a detector like the prototype for MARS can provide sufficient information for position determination. The requirements for pulse shape analysis having (a) a pronounced dependence of shape and amplitude (for the transient signals) of the pulses on the position of the interaction (dynamic behaviour) and (b) transient signals with amplitudes yielding a useful signal-to-noise ratio are fulfilled for interactions in most parts of the detector. However, unavoidably in all parts of the detector positions exist where points of interaction induce tiny or even vanishing transient signals.

The amplitudes of the transient signals depend on the distance between the interaction point and the sensing neighbouring segment. Therefore, a detector with more and hence smaller segments should, at first sight, provide larger amplitudes. However, it was already demonstrated in the discussion of the front segment that smaller segments result in weighting fields with smaller extension (see Fig. 17). Since the range of coordinates (z,φ) is smaller for smaller segments, the dynamic behaviour of the signals will be increased, but the amplitudes remain the same or are even somewhat smaller. The question whether the response of a detector can be improved or will be deteriorated by using other layouts of segmentation, i.e. other sizes and arrangements of segments, or other shapes of the crystal, will be addressed in detail in a further publication.

All these features have to be considered in the application of pulse shape analysis for position determination. Although we have restricted the aim of this paper to discuss signals originating from single interactions, it is clear that only an analysis of the signals from all segments, net charge as well as transient signals, resulting in a consistent interpretation can achieve the best possible position resolution.

The algorithms for pulse shape analysis have to extract (a) the number of interaction points and (b) the three-dimensional position and deposited energy for each of them. For this task, we are applying methods of artificial intelligence, artificial neural networks (ANN) and genetic algorithms (GA), as it will be demonstrated in an upcoming publication [7,26]. Usually, there is more than one interaction point in the detector or even in one segment and the measurable signals are the sum of the signals originating from the individual interactions. Clearly, these signals can be disentangled only if a pronounced dependence of the signals on the positions of the individual interactions exists.

Acknowledgements

This work was supported by the Commission of the European Union within the TMR Program under contract no. ERBFMRXCT97-0123 and, partly, by the Deutsche Forschungsgemeinschaft under contract no. KR 1796/1-1.

References

[1] C. Rossi-Alvarez, Nucl. Phys. News 3 (3) (1993) 10.
[2] J. Simpson, Z. Phys. A 358 (1997) 139.
[3] M.A. Deleplanque, R.M. Diamond (Eds.), GAMMASPHERE Proposal, Lawrence Berkeley National Laboratory, Report 5202, 1988.
[4] I.Y. Lee, Nucl. Instr. and Meth. A 422 (1999) 195.
[5] M.A. Deleplanque et al., Nucl. Instr. and Meth. A 430 (1999) 292.
[6] D. Bazzacco for the MARS collaboration, Workshop on GRETA Physics, Berkeley, LBNL-41700 CONF-980228, 1998.
[7] MARS Homepage: http://axpd30.pd.infn.it/MARS.
[8] Homepage of the TMR network "Gamma-ray tracking detectors": http://ikp193.ikp.kfa-juelich.de/tmr98/.
[9] G.J. Schmid et al., Nucl. Instr. and Meth. A 430 (1999) 69.
[10] J. van der Marel, B. Cederwall, Nucl. Instr. and Meth. A 437 (1999) 538.
[11] D. Bazzacco, private communication.
[12] M. Eschenauer et al., Nucl. Instr. and Meth. A 340 (1994) 364.
[13] Th. Kröll et al., Nucl. Instr. and Meth. A 371 (1996) 489.
[14] B. Philhour et al., Nucl. Instr. and Meth. A 403 (1998) 136.
[15] G.J. Schmid et al., Nucl. Instr. and Meth. A 422 (1999) 368.
[16] E. Gatti et al., Nucl. Instr. and Meth. 193 (1982) 651.
[17] G.F. Knoll, Radiation Detection and Measurement, Wiley & Sons, Singapore, 1989.
[18] E. Gatti et al., IEEE Nucl. Sci. Symp., Seattle, 1999.
[19] Diffpack v1.4 (http://www.nobjects.com), 1996.
[20] T.W. Raudorf et al., IEEE Trans. Nucl. Sci. NS-29 (1982) 764.
[21] G. Ottaviani et al., IEEE Trans. Nucl. Sci. NS-22 (1975) 192.
[22] L. Mihailescu et al., Nucl. Instr. and Meth. A 447 (2000) 350.
[23] V. Radeka, Ann. Rev. Nucl. Part. Sci. 38 (1988) 217.
[24] J. Eberth et al., Nucl. Instr. and Meth. A 369 (1996) 135.
[25] K. Vetter et al., Nucl. Instr. and Meth. A 452 (2000) 105, 223.
[26] Th. Kröll et al., in preparation.